

AN EXTREME PULSAR TAIL PROTRUDING FROM THE FRYING PAN SUPERNOVA REMNANT

C.-Y. NG^{1,2,7,8}, N. BUCCIANTINI^{3,4}, B. M. GAENSLER², F. CAMILO⁵, S. CHATTERJEE⁶, AND A. BOUCHARD¹

ApJ, in press

ABSTRACT

The Frying Pan (G315.9–0.0) is a radio supernova remnant with a peculiar linear feature (G315.78–0.23) extending 10′ radially outward from the rim of the shell. We present radio imaging and polarization observations obtained from the Molonglo Observatory Synthesis Telescope and the Australia Telescope Compact Array, confirming G315.78–0.23 as a bow-shock pulsar wind nebula (PWN) powered by the young pulsar J1437–5959. This is one of the longest pulsar tails observed in radio and it has a physical extent over 20 pc. We found a bow-shock stand-off distance of 0.002 pc, smallest among similar systems, suggesting a large pulsar velocity over 1000 km s^{−1} and a high Mach number ∼200. The magnetic field geometry inferred from radio polarimetry shows a good alignment with the tail orientation, which could be a result of high flow speed. There are also hints that the postshock wind has a low magnetization and is dominated by electrons and positrons in energy. This study shows that PWNe can offer a powerful probe of their local environment, particularly for the case of a bow shock where the parent supernova shell is also detected.

Subject headings: ISM: individual (G315.78–0.23, G315.9–0.0) — ISM: supernova remnants — pulsars: individual (PSR J1437–5959) — radio continuum: ISM — stars: neutron — stars: winds, outflows

1. INTRODUCTION

Neutron stars are born with large space velocities of a few hundred kilometers per second. They eventually escape their natal supernova remnants (SNRs) after ∼ 10⁵ yr and travel supersonically through the interstellar medium (ISM), which typically has a sound speed of 1–10 km s^{−1} in the cold and warm phases. In this case, the pulsars’ relativistic outflows are confined by ram pressure of the ISM, resulting in bow-shock pulsar wind nebulae (PWNe). These systems exhibit cometary morphologies with long tails, and emit broadband synchrotron radiation from radio to X-rays (see, Gaensler & Slane 2006, for a review). As compared to PWNe within SNRs, bow-shocks are governed by simpler boundary conditions, therefore, providing a powerful probe of the local ISM environment.

At radio frequencies, PWNe generally show a larger extent than their X-ray counterparts, due to long synchrotron cooling timescale of radio-emitting particles, which can be up to 10⁵–10⁶ yr. Therefore, radio PWNe can act as direct calorimeters to reflect the integrated history of the systems. Table 1 lists the longest pulsar tails detected in radio. The best example is the Mouse PWN, its morphology consists of a broad cone-

shaped outer region and a collimated narrow inner region, which were suggested to be postshock flows from the forward and backward termination shocks, respectively (Gaensler et al. 2004). Radio observations of PWNe also reveal the nebular magnetic field structure via polarimetry. Previous studies indicate a diverse *B*-field configuration among bow-shock PWNe, from a helical field perpendicular to the tail (Ng et al. 2010) to a *B*-field parallel to the tail (Yusef-Zadeh & Gaensler 2005), but the origin of the variation remains a puzzle.

The “Frying Pan” SNR (G315.9–0.0) is a faint 15′-diameter radio shell with an intriguing 10′ linear protrusion, G315.78–0.23 (the “handle”), extending northwest from the rim, such that the overall morphology resembles a Frying Pan (see Figure 1). Based on the lack of an IR counterpart, Whiteoak & Green (1996) concluded that the radio emission is nonthermal and the source is an SNR. In this case, we suggested that the highly unusual linear feature is due to the trailing relativistic wind of a fast pulsar moving outward from the central birth place. We have recently performed a deep radio search near the tip of the protrusion and discovered a new radio pulsar, J1437–5959, providing strong support to the above picture (Camilo et al. 2009). This pulsar has a short period of 61.7 ms, a characteristic age of 110 kyr, and a high spin-down power $\dot{E}=1.5 \times 10^{36}$ ergs^{−1}. While its large dispersion measure of 549 pc cm^{−3} suggests a distance of 8 kpc, as Camilo et al. (2009) noted, the estimate is uncertain and could be easily off by 25%.

In this paper, we focus on the handle of the Frying Pan and establish its PWN nature using new and archival radio observations from the Molonglo Observatory Synthesis Telescope (MOST) and the Australia Telescope Compact Array (ATCA). Its projected length over 20 pc makes it one of the longest pulsar tails observed. We show that this unique object can provide crucial information on the pulsar environment that is not easily ac-

ncy@physics.mcgill.ca

¹ Department of Physics, McGill University, Montreal, QC H3A 2T8, Canada

² Sydney Institute for Astronomy, School of Physics, The University of Sydney, NSW 2006, Australia

³ NORDITA, Albanova Research Center, Roslagets backen 23, 106 91 Stockholm, Sweden

⁴ INAF – Osservatorio Astrofisico di Arcetri, Largo E. Fermi 5, 50125 Firenze, Italy

⁵ Columbia Astrophysics Laboratory, Columbia University, New York, NY 10027, USA

⁶ Astronomy Department, Cornell University, Ithaca, NY 14853, USA

⁷ Tomlinson Postdoctoral Fellow

⁸ CRAQ Postdoctoral Fellow

TABLE 1
LONG PULSAR TAILS IN RADIO, SORTED IN PHYSICAL LENGTH

PWN	SNR	PSR/Neutron Star	Length (pc)	Velocity (km s^{-1})	Distance ¹ (kpc)	Reference
G315.78–0.23	Frying Pan	J1437–5959	20	~1000	8	This work
Mouse	...	J1747–2958	16	300	5	1,2
G319.9–0.7	...	J1509–5850	10	300	3	3,4
G68.77+2.82	CTB 80	B1951+32	5	274	2	5,6
G34.56–0.50	W44	B1853+01	2	375	2.6	7
Duck	...	B1757–24	1.5	<360	5.2	6
G47.38–3.88	...	B1929+10	1.3	177	0.36	8,9
G189.23+2.90	IC 443	J061705.3+222127	1	230	1.5	10,11
N157B ²	N157B	J0537–6910	30	?	50	12
G309.92–2.51 ³	...	J1357–6429	7	?	2.5	13

REFERENCES. — (1) Gaensler et al. (2004); (2) Hales et al. (2009); (3) Kargaltsev et al. (2008); (4) Ng et al. (2010); (5) Castelletti et al. (2003); (6) Zeiger et al. (2008); (7) Frail et al. (1996); (8) Chatterjee et al. (2004); (9) Becker et al. (2006); (10) Olbert et al. (2001); (11) Gaensler et al. (2006); (12) Lazendic et al. (2000); (13) Chang et al. (2011).

¹ All distance estimates are subject to large uncertainties, except for PSR B1929+10, which is obtained from parallax.

² This system is more likely to be a PWN crushed by the SNR reverse shock, instead of a bow-shock (van der Swaluw 2004; Chen et al. 2006).

³ The radio counterpart is not confirmed.

cessible in other systems.

2. OBSERVATIONS AND DATA REDUCTION

We carried out new radio imaging observations of the Frying Pan with the ATCA at 3 and 6 cm in four different array configurations, and processed archival ATCA data at 13 and 20 cm, including those from the Southern Galactic Plane Survey (Haverkorn et al. 2006). Table 2 lists the parameters of all datasets used in this study. The last two observations in the list were carried out after the Compact Array Broadband Backend (CABB) upgrade (Wilson et al. 2011), which provides 2 GHz bandwidth, nearly 20 times improvement over the pre-CABB era. Note that with such a large bandwidth, the 3 and 6 cm data and images we refer to throughout this paper actually cover 3.0–3.7 cm and 4.7–6.6 cm, respectively. The pre-CABB observations at 3 and 6 cm were made with a two-pointing mosaic to cover 5' from the tip of G315.9–0.0. One more pointing was added in the CABB observations to extend the coverage over the entire 8'-handle. The flux density scale is set by observations of the primary calibrator, PKS B1934–638. A secondary calibrator, PKS B1414–59, which is 2'.4 away from our source, was observed every 30 minutes to determine the antenna gains.

All data reduction was performed using the MIRIAD package⁹. After discarding the edge channels and channels affected by self-interference, we obtained a usable bandwidth of 104 MHz and 1848 MHz for the pre-CABB and CABB data, respectively, at each wavelength. The longest baselines in the 13 and 20 cm data were excluded to provide a uniform u - v coverage. We examined the visibility data to reject bad data points due to poor atmospheric phase stability, then applied gain, bandpass, flux, and polarization calibrations. Mosaiced intensity maps were formed using the multifrequency synthesis technique with uniform weighting at 13 and 20 cm and with natural weighting at 3 and 6 cm. The maps are de-

convolved using a maximum entropy algorithm (MOSMEM; Sault et al. 1999) and restored with Gaussian beams of FWHM $23'' \times 20''$ at 20 cm, $12'' \times 9''.7$ at 13 cm, and $3''.7 \times 3''.3$ at both 3 and 6 cm. The final maps have rms noise of 1, 0.1, 0.011, and 0.016 mJy beam⁻¹ at 20, 13, 6, and 3 cm, respectively. While the last two values are very close to the theoretical limits, the 20 cm map is severely contaminated by a strong source nearby and the noise in the 13 cm map is also slightly higher than the theoretical level of 0.06 mJy beam⁻¹.

For polarimetry, we only focused on the 3 and 6 cm data since the other observations lack the sensitivity and suffer from beam depolarization. To mitigate the problem of bandwidth depolarization due to the large fractional bandwidth of CABB data, we divided the 6 cm CABB data into 33 sub-bands (56 MHz each) and the pre-CABB data into 2 sub-bands. The problem is less severe at 3 cm, therefore, we only divided the CABB data into 5 sub-bands. Individual Stokes Q and U maps for the sub-bands are formed using the same procedure as above for Stokes I. We attempted to apply the rotation measure (RM) synthesis technique (Brentjens & de Bruyn 2005) to determine the foreground Faraday rotation. Although the result is generally consistent with the pulsar RM reported by Camilo et al. (2009), the uncertainty is too large to be useful. Therefore, we adopted the pulsar value of $-700 \pm 25 \text{ rad m}^{-2}$ to derotate the individual Stokes Q and U maps. The error in RM corresponds to uncertainties of 1°.5 and 4°.3 in the polarization angles at 3 and 6 cm, respectively. Finally, the derotated maps in each frequency channel were weighted according to their rms noise and co-added to generate maps of polarized intensity and position angle.

In addition to the radio observations, we also processed the *Fermi* Large Area Telescope data to search for pulsations in γ -rays. We carried out the analysis using the Fermi Science Tools v9r18p6 and considered only the “diffuse” class of events with a cut at zenith angles $>105^\circ$. We only used the first year of *Fermi* data taken before 2009 September 27, when the pulsar ephemeris

⁹ <http://www.atnf.csiro.au/computing/software/miriad/>

TABLE 2
PARAMETERS FOR THE ATCA OBSERVATIONS OF G315.9–0.0

Obs. Date	Array Configuration	Center Frequency (MHz)	Usable Bandwidth (MHz) ¹	No. of Channels ¹	Integration Time (hr)
1998 Jul 5	750E	1384, 2496	104	13	11
1998 Dec – 2000 Aug ²	various ²	1384	104	13	0.33
1999 Mar 25	1.5B	1384, 2496	104	13	12
1999 Apr 20	1.5C	1384, 2496	104	13	12
2008 Jul 23	H214	1344, 1436	104	13	9
2008 Dec 8	750B	4800, 8640	104	13	11.5
2009 Feb 18	EW352	4800, 8640	104	13	12
2009 Jun 13	6A	5500, 9000	1848	1848	12
2009 Jul 31	1.5A	5500, 9000	1848	1848	12.5

¹ Per center frequency.

² Part of the Southern Galactic Plane Survey (Haverkorn et al. 2006).

given by Camilo et al. (2009) is valid. We extracted 0.1–10 GeV photons within 1° of the pulsar position, applied the barycentric correction to their arrival times, and folded them according to the radio ephemeris. However, no pulsation is detected. This is not unexpected given the large pulsar distance.

3. RESULTS

3.1. Overall Morphology and Flux Densities

Figure 1 presents radio continuum images of the Fry-ing Pan at 36, 20, 13, 6 and 3 cm. All of them were taken with the ATCA as described in Section 2 except the 36 cm one, which is from the MOST Supernova Remnant Catalogue¹⁰ (Whiteoak & Green 1996). The 13 cm image has been reported in our previous paper (Camilo et al. 2009). The radio shell exhibits a circular morphology with inner and outer radii of $4.5'$ and $7'$, respectively. The overall shell is brighter to the west, particularly in the northwest where it intersects with the pulsar tail, but it is very faint and diffused to the northeast. Excluding the handle, the shell has flux densities of 0.4 ± 0.1 and 0.5 ± 0.1 Jy at 36 and 13 cm, respectively. The image at 20 cm is severely contaminated by strong sources nearby, precluding any detailed flux measurement. Also, the 3 and 6 cm observations were designed to map the tip of the linear protrusion, hence, they are insensitive to the overall SNR structure.

As shown in Figure 1, the handle is highly collimated and extends $8.5'$ from the shell to the pulsar, at a position angle of 314° (north through east). It has a width of $6''$ at the tip, which is only resolved in the 3 and 6 cm images, then gradually widens to $\sim 60''$ at the intersection with the shell. At the source distance of 8 ± 2 kpc, these correspond to a physical length of 20 ± 5 pc and width from 0.23 ± 0.06 pc to 2.3 ± 0.6 pc. Beyond $5'$ from the pulsar, the 3 cm emission falls below the observation sensitivity. We note that extrapolating the handle inside the remnant slightly misses the shell's geometric center by $\sim 1.5'$ to the northeast.

The entire handle has flux densities of 110 ± 40 , 35 ± 1 , 26 ± 10 and 18 ± 5 mJy at 36, 13, 6, and 3 cm, respectively. These measurements have large uncertainties due to strong variation in the diffused background. Therefore, we did not attempt to derive the radio spectra index from them, instead, we employed the spectral tomogra-

phy technique between the 3 and 6 cm data. We followed a similar procedure as described by Gaensler & Wallace (2003) and smoothed the maps to $10''$ resolution to boost the signal-to-noise ratio. We found a spectral index $\alpha = -0.45 \pm 0.1$ (defined as $S_\nu \propto \nu^\alpha$), but no significant spatial variation of α .

3.2. The Handle

Figures 2(a) and (b) show the 3 and 6 cm intensity maps zoomed-in near the pulsar. The detailed morphology of the handle is very similar at both wavelengths. There is a hint of unresolved compact emission at the pulsar position at 6 cm (see the contours in Figure 2(c)) with a flux density $60 \pm 30 \mu\text{Jy}$. However, this is not observed at 3 cm. The radio emission of the handle peaks at $45''$ from the pulsar, with flux densities of 0.25 and 0.20 mJy beam⁻¹ at 6 and 3 cm, respectively. Further away, there is a kink at $1'$ from the pulsar, such that the handle changes orientation by 34° and runs towards east for $10''$, then switches back to the original direction. The reverse occurs around $30''$ further southeast. As a net result, a $40''$ -long section is displaced by $6''$ to the northeast.

For polarimetry results, the polarization B -vectors, after correcting for foreground Faraday rotation, are overplotted in Figures 2(a) and (b). These indicate a highly ordered magnetic field structure. The B -field well aligns with the handle's elongation, and changes direction along with the handle across the kink. Farther from the kink, the field orientation remains constant until the polarization signal falls below detection beyond $2.4'$ from the pulsar. Figures 2(c) and (d) show the polarized intensity maps at 6 and 3 cm. The polarized emission generally follows the total intensity, except across the kink, where it shows a slight depolarization. We estimate that the polarization fraction is up to $\sim 40\%$ and $\sim 50\%$ at 6 and 3 cm, respectively. A reduced polarization fraction at lower frequency has been observed in other sources (e.g., Ng et al. 2010) and it could be attributed to beam depolarization. However, we note that these values are rough estimates due to high background. Also, variations in polarization angle could shift power in the polarized image into smaller scales, to which the interferometric observations are more sensitive (see discussion in Gaensler et al. 1999). Therefore, the absolute polarized flux could be biased and the maps should be taken as relative measurements only.

¹⁰ <http://www.physics.usyd.edu.au/sifa/Main/MS>

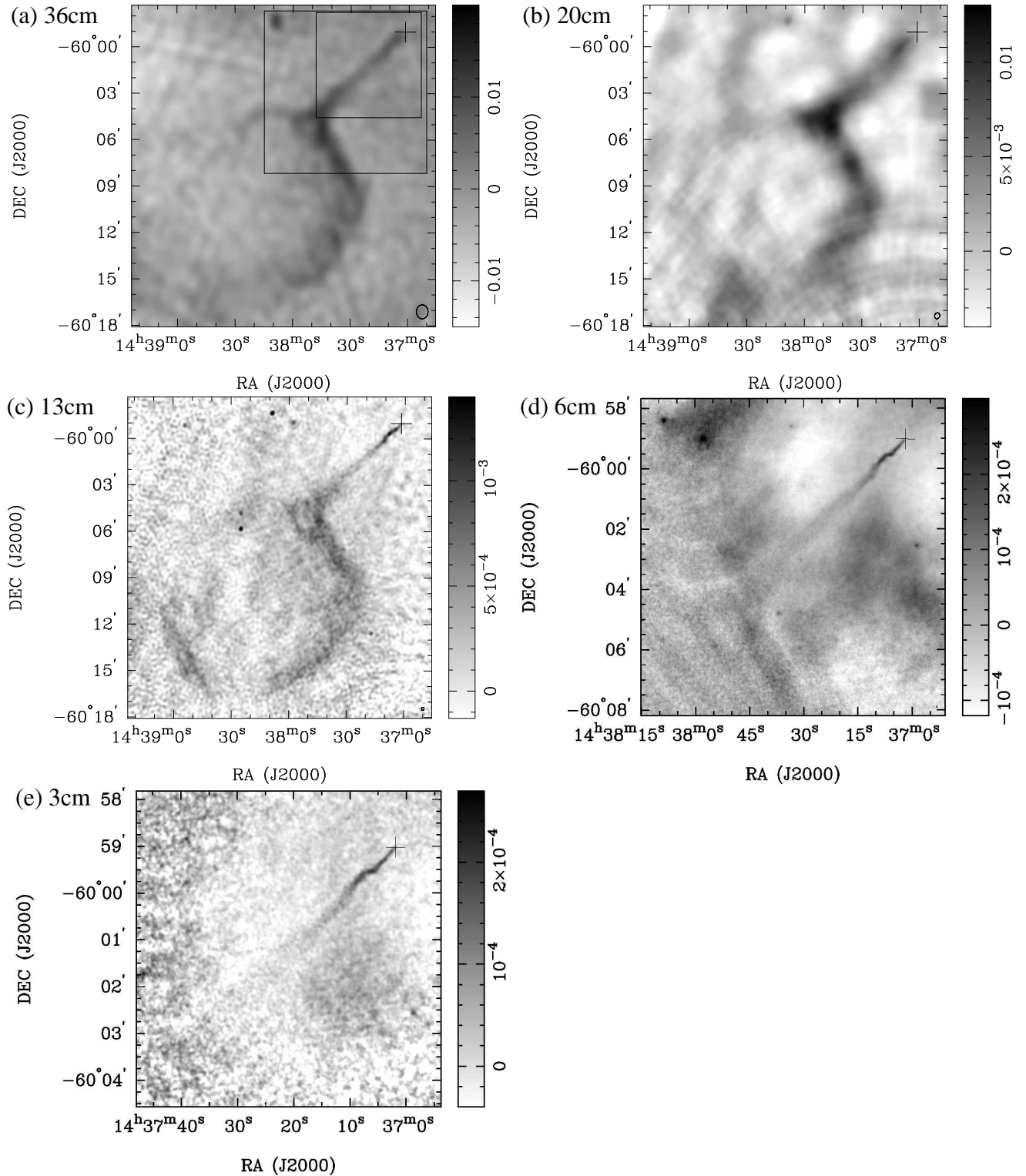


FIG. 1.— Radio continuum images of G315.9–0.0 at different wavelengths. The 36 cm image is adopted from the MOST Supernova Remnant Catalogue (Whiteoak & Green 1996) and the rest are taken with ATCA. The large and small boxes in the 36 cm image indicate the field of views of the 6 and 3 cm images, respectively. Position of PSR J1437–5959 [(J2000.0) R.A.=14^h37^m01^s.91(3), decl.=–59°59′01″.4(3) (Camilo et al. 2009)] is marked by the cross. The restoring beams are shown at the lower right of each panel. The gray scales are linear with the scale bars in units of Jy beam^{–1}. The 13 cm map is same as the one reported in Camilo et al. (2009).

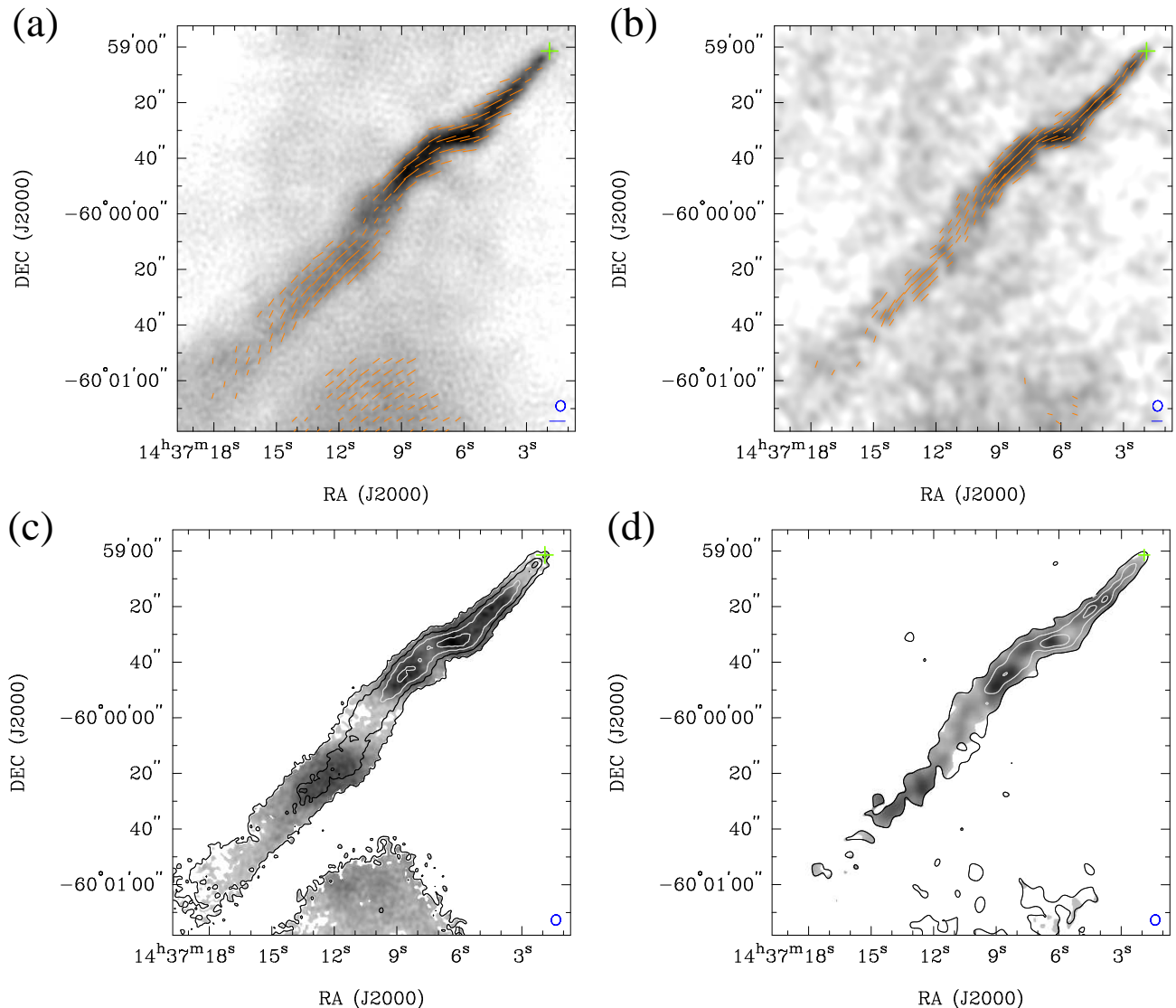


FIG. 2.— Top: radio continuum images of the tip of G315.9–0.0 at: (a) 6 cm and (b) 3 cm, overlaid with the corresponding polarization B -vectors that show the intrinsic magnetic field orientation. The gray scales are linear, ranging from -0.045 to $0.22 \text{ mJy beam}^{-1}$ at 6 cm and from -0.02 to $0.3 \text{ mJy beam}^{-1}$ at 3 cm. The vector lengths are proportional to the polarized intensity, with the scale bars at the lower right representing $0.1 \text{ mJy beam}^{-1}$. Bottom: linear polarized emission at: (a) 6 cm and (b) 3 cm, overlaid with total intensity contours at levels of 0.03 , 0.073 , 0.15 , and $0.22 \text{ mJy beam}^{-1}$ for 6 cm and 0.06 , 0.12 , and $0.17 \text{ mJy beam}^{-1}$ for 3 cm. The gray scales are linear, ranging from 0 to $0.15 \text{ mJy beam}^{-1}$ at 6 cm and from 0 to $0.2 \text{ mJy beam}^{-1}$ at 3 cm. In all panels, position of PSR J1437–5959 is marked by the cross and the restoring beams are shown at the lower right.

4. DISCUSSION

4.1. Nature of the Handle and Its Association with the SNR

Our results show that the handle of the Frying Pan (G315.78–0.23) has a high degree of linear polarization with a flat radio spectrum, hence confirming that it is a PWN powered by PSR J1437–5959. If the source is at a distance of 8 kpc, then it would have a physical length over 20 pc, the longest pulsar tail ever detected. The source morphology suggests that it is a bow shock with the pulsar traveling highly supersonically in the ISM. As radio PWNe generally have a very long lifetime (see Equation (10) below), the fact that the tail points toward the general direction of the remnant center argues for an association between PSR J1437–5959 and G315.9–0.0 (but see, Zeiger et al. 2008). We performed Monte Carlo

simulations to quantify the probability of chance association. We employed a realistic population synthesis model (Faucher-Giguère & Kaspi 2006; A. Bouchard et al. 2012, in preparation) and found that at this sky position, an average of 0.2 field radio pulsars are expected within $20'$ from the shell, younger than 10^6 yr and with a radio flux larger than that of PSR J1437–5959. If we further require the pulsar’s projected motion in the past to intercept any part of the shell, then the number greatly reduces to 0.0012, therefore, strongly suggesting an association between PSR J1437–5959 and the Frying Pan. Although the tail does not point toward the exact geometry center of the shell, this is not uncommon and could be the result of asymmetric supernova explosion, the progenitor’s proper motion, or a slight gradient in the ISM density (see, Gvaramadze 2006; Ng et al. 2007; Vigelius et al. 2007).

To estimate the kinematics of the system, we extrapolate the tail inside the shell and take the closest approach to the center as the supernova site, which is 14.5 away from the pulsar location. This implies a distance $l = 1.0 \times 10^{20} d_8$ cm traveled by the pulsar since birth, at the source distance of $8 d_8$ kpc. Here we assume the pulsar motion lies in the plane of the sky for simplicity. The pulsar velocity v_* and age t are then related by $v_* = l/t$. Even if the pulsar travels as fast as 2000 km s^{-1} , the system would still be older than 15 kyr , such that G315.9–0.0 has long passed the free expansion phase. On the other hand, the transition from the Sedov phase to the snowplow phase occurs at $t_{\text{tr}} \approx 29 E_{51}^{4/17} n_0^{-9/17} \text{ kyr}$ with a shell radius $R_{\text{tr}} \approx 19.1 E_{51}^{5/17} n_0^{-7/17}$, where E_{51} is the supernova explosion energy in units of 10^{51} erg and n_0 is the ISM number density in cm^{-3} (Blondin et al. 1998). Our observed shell radius of $7'$ gives a physical size $R = 16.3 d_8 \text{ pc}$, slightly smaller than R_{tr} for the typical values of $E_{51} = 1$ and n_0 between 0.1 and 1 . Therefore, we adopt the Sedov solution

$$R = 1.15 \left(\frac{E_0 t^2}{\rho} \right)^{1/5}, \quad (1)$$

where $E_0 = 10^{51} E_{51} \text{ erg}$ and ρ is the ISM density in g cm^{-3} .

4.2. Pulsar Velocity and Age

The bow-shock stand-off distance r_{bs} ahead of the PWN is determined by the ram pressure balance between the pulsar wind and the ISM. For isotropic wind,

$$\rho v_*^2 = \frac{\dot{E}}{4\pi c r_{\text{bs}}^2}. \quad (2)$$

Assuming a constant ρ across the field, we can solve Equations (1) and (2) to obtain

$$r_{\text{bs}} = \left(\frac{\dot{E}}{4\pi c E_0 l^2} \right)^{1/2} \left(\frac{R}{1.15} \right)^{5/2} = 0.0024 d_8^{3/2} E_{51}^{-1} \text{ pc}. \quad (3)$$

This corresponds to an angular scale $0''.06 d_8^{1/2} E_{51}^{-1}$, too small to be resolved by the observations. It is interesting to note that this value is independent of the system age, pulsar velocity and ambient density. Also, it is one of the smallest stand-off distances among bow-shock PWNs, e.g., an order of magnitude smaller than that of the Mouse (Gaensler et al. 2004). This indicates either a very large Mach number or a very dense ambient medium. We argue that the latter case is less likely, since the CO map (Dame et al. 2001) shows no evidence of molecular clouds in the region. As mentioned, there is a marginal detection of a compact feature at the tip of the PWN with a flux density $60 \pm 30 \mu\text{Jy}$ at 6 cm . If this is from the pulsar, then comparing to the pulsed flux density of $75 \mu\text{Jy}$ at 20 cm (Camilo et al. 2009) indicate a rather flat radio spectrum. As an alternative, this could also be the surface of the backward termination shock, which has an extent of $5 r_{\text{bs}}$ according to hydrodynamic simulations (Gaensler et al. 2004), such a small-scale structure would not be resolved in our images. Further observations with high time resolution

could distinguish between these cases. Finally, we note that the PWN half-width near the tip is about $40 r_{\text{bs}}$, much greater than the value found in magnetohydrodynamic (MHD) simulations (Bucciantini et al. 2005). The discrepancy could possibly be due to anisotropy of the pulsar wind or mass loading through contamination (see Vigelius et al. 2007; Romani et al. 2010; Lyutikov 2003).

Assuming cosmic abundances, we substitute r_{bs} into Equation (2) to obtain

$$v_* = 1700 E_{51}^{1/2} d_8^{-3/2} n_0^{-1/2} \text{ km s}^{-1} \quad (4)$$

and hence

$$t = 19 E_{51}^{-1/2} d_8^{5/2} n_0^{1/2} \text{ kyr}. \quad (5)$$

While we argue above that n_0 cannot be too high, n_0 cannot be too low either because of the detection of the radio shell in G315.9–0.0, hence, we can rule out the hot ISM phase. For a typical value of n_0 between 0.1 and 1 in the warm ISM phase, the inferred velocity would be nearly 2000 km s^{-1} with a young system age in the order of 10 kyr , as proposed by Camilo et al. (2009). This indicates $t < t_{\text{tr}}$, providing support to the Sedov phase for the SNR. We also note that the age estimate is much younger than the pulsar's characteristic age of 110 kyr , which could be reconciled if the pulsar was born with a spin period close to the present-day value (see Ng et al. 2007). With these results, we can estimate the pressure P_{head} at the head of the bow shock and the pulsar Mach number \mathcal{M} using

$$\gamma P_{\text{ISM}} \mathcal{M}^2 = P_{\text{head}} = \rho v_*^2 = 6.8 \times 10^{-8} E_{51} d_8^{-3} \text{ dyn cm}^{-2}, \quad (6)$$

where P_{ISM} is the ambient pressure and $\gamma = 5/3$ is the ISM adiabatic index. Since different phases of the ISM are generally in pressure equilibrium, P_{ISM} should be more uniform than ρ , hence, the Mach number estimate would be more certain than the pulsar velocity estimate (see the detailed discussion by Kargaltsev et al. 2008). A typical ISM pressure of $10^{-12} \text{ dyn cm}^{-2}$ (corresponding to $P_{\text{ISM}}/k = 7250 \text{ cm}^{-3} \text{K}$) gives $\mathcal{M} = 200 E_{51}^{1/2} d_8^{-3/2}$, suggesting a highly supersonic pulsar motion. For smaller values of P_{ISM} (e.g., Ferrière 2001; Cox 2005), the inferred Mach number would be even higher. While such a highly supersonic motion is expected to produce a very sharp Mach cone with a small half-opening angle $\theta \sim \sin^{-1}(1/200)$, the observed width of the tail increases from $6''$ to $60''$ over its entire length of $7'$, implying $\theta \sim \sin^{-1}(1/15)$. The discrepancy could be the result of overpressure in the tail, such that

$$\begin{aligned} P_{\text{tail}} &\sim \rho (v_* \sin \theta)^2 = P_{\text{head}} \sin^2 \theta \\ &= P_{\text{head}}/15^2 = 0.004 P_{\text{head}}. \end{aligned} \quad (7)$$

See Section 4.5 below for further discussion.

4.3. The Kink

Figure 2 shows a kink in the tail at $1'$ from the pulsar. We argue that this is unlikely caused by flow instability or by a global ISM pressure gradient, since the magnetic field is highly ordered across the kink and the tail resumes its original orientation further downstream. Instead, it could be the result of interstellar turbulence. Comparing the kink's $6''$ -lateral displacement to its $1'$ -separation from the pulsar, we can deduce a turbulent

velocity $v_t = (6''/1')v_* = 0.1v_*$, which is much higher than the typical sound speed of $\sim 10 \text{ km s}^{-1}$ in the warm ISM phase, giving evidence of supersonic turbulence. As this PWN system has a rather high flow speed (see Section 4.5 below), the postshock wind could become compressible. The compression by the ISM turbulence would result in enhanced synchrotron emissivity, which could naturally explain the coincidence of the kink and the radio peak. Also, it would introduce disorder in the magnetic field, reducing the polarized fraction near the kink as observed.

4.4. Magnetic Field Strength

To estimate the magnetic field strength in the PWN, we define $k_m = U_B/U_p$ to be the magnetization of the postshock wind, i.e., the ratio between the magnetic and relativistic particle (electron+ion) energy densities (see Pavlov et al. 2003). MHD simulations show a relatively uniform magnetization in the tail with k_m of the typical order of 0.1 (Bucciantini et al. 2005). Let η be the ion to electron energy density ratio, we then have $U_p = (1 + \eta)U_e$ and we can estimate the average magnetic field strength B from standard synchrotron theory

$$\frac{U_B}{k_m(1 + \eta)} = U_e = c_{12}B^{-3/2}L/V, \quad (8)$$

where c_{12} is a constant that depends weakly on the spectral index and on the lower and upper frequency limits of the emission (see Pacholczyk 1970) and L/V is the synchrotron volume emissivity. Assuming a simple power-law spectrum between 10^7 and 10^{13} Hz as in Ng et al. (2010), our measured flux density and spectral index yield

$$B = \left[8\pi c_{12} k_m (1 + \eta) \frac{L}{V} \right]^{2/7} = 60 k_m^{2/7} (1 + \eta)^{2/7} d_8^{-2/7} \mu\text{G}. \quad (9)$$

We note that this result is insensitive to the frequency limits, and to k_m and η . For example, changing the upper limit to 10^{11} Hz only lowers B by 13%. If we ignore any ions (i.e., $\eta = 0$) and take $k_m = 0.1$, we obtain $B = 30 \mu\text{G}$. Adopting $k_m = 0.01$ yields $B = 16 \mu\text{G}$, while the equipartition case ($k_m \approx 1$) gives $B = 60 \mu\text{G}$. For emission at 6 cm ($\nu \approx 5$ GHz), the synchrotron lifetime is

$$t_{\text{syn}} = 18B^{-3/2} \nu^{-1/2} \text{ kyr} = 540 k_m^{-3/7} (1 + \eta)^{-3/7} d_8^{3/7} \text{ kyr}, \quad (10)$$

sufficiently longer than the estimated age of the system (see Equation (5)). Comparing to the synchrotron cooling, inverse Compton scattering with the cosmic microwave background is negligible. Therefore, the radio PWN should trace the pulsar motion over a long time, providing support to the association with G315.9–0.0.

4.5. Pressure and Flow speed

The magnetic field estimate can give us a handle on P_{ISM} , which consists of the magnetic pressure and the particle pressure. Taking the pulsar wind as relativistic ideal gas, the particle pressure is given by $U_p/3$, hence,

$$P_{\text{tail}} = \frac{B^2}{8\pi} + \frac{U_p}{3} = \left(1 + \frac{1}{3k_m}\right) \frac{B^2}{8\pi} = 1.5 \times 10^{-10} \left(1 + \frac{1}{3k_m}\right) k_m^{4/7} (1 + \eta)^{4/7} d_8^{-4/7} \text{ dyn cm}^{-2}. \quad (11)$$

This confirms that the system is highly overpressured as compared to the environment. To match P_{tail} we derived in Equation (7), it would require $\eta < 1$ and $k_m \sim 0.02$, hence, this gives some hints that the postshock wind is dominated by electrons and positrons with a small magnetization. Finally, we note that P_{tail} above is much lower than the value $0.02P_{\text{head}}$ found in MHD simulations (Bucciantini et al. 2005), although those simulations only extend for a few r_{bs} in the tail direction.

We can estimate the average flow speed v_f of the postshock wind based on energy conservation. If we assume the pulsar spin-down energy all converts into the magnetic and particle kinetic energy downstream, then

$$\dot{E} = A(v_f + v_*)(U_B + U_p) = A(v_f + v_*) \left(1 + \frac{1}{k_m}\right) \frac{B^2}{8\pi}, \quad (12)$$

where A is the tail's cross-sectional area. We modeled the tail with a truncated cone of diameter from $6''$ to $60''$, then A scales with the distance z (in arcminutes) from the pulsar as $A(z) \approx 4.0 \times 10^{35} (1 + 1.1z)^2 d_8^2 \text{ cm}^{-2}$, giving

$$v_f \approx 2.3 \times 10^5 (1 + 1.1z)^{-2} \frac{k_m^{3/7}}{1 + k_m} (1 + \eta)^{-4/7} d_8^{-10/7} \text{ km s}^{-1}, \quad (13)$$

here v_* is ignored as it is negligible. Our result indicates a rather high flow speed near the pulsar ($z \lesssim 1$): for $\eta = 0$ and $k_m = 0.1$, we obtain $v_f \approx 0.06c$. If $k_m = 0.01$, then v_f is a factor of 2.5 lower. These numbers are slightly higher than those observed in other bow-shock PWN systems (e.g., Gaensler et al. 2004; Kargaltsev et al. 2008), but lower than the simulation prediction (Bucciantini et al. 2005). We note that while synchrotron loss is negligible, other energy dissipation mechanisms, e.g., induced by flow instability, mass-loading or ions in the wind, could significantly reduce the flow speed (see Lyutikov 2003). Combining our radio results with future X-ray observations can provide a more complete picture of the particle spectrum, thus, better accounting for the total energetics of the wind to reveal the flow structure. Spatially-resolved X-ray spectroscopy can also indicate any deceleration in the flow. For particles emitting in the X-ray range ($\nu \sim 5 \times 10^{17}$ Hz), Equation (10) gives a synchrotron cooling time of 150 yr. Hence, a flow speed of $0.06c$ would result in a 3 pc-long X-ray PWN, comparable to other long X-ray tails (Kargaltsev et al. 2008).

4.6. Comparison with Other Long Pulsar Tails in Radio

In Table 1, we summarize the physical extents and space velocities of the longest pulsar tails detected in radio. We found only a very weak correlation between these two quantities. This is not surprisingly, since we expect that the radio emission should also depend on the physical conditions of the local environment, such as ambient density and magnetic field. The three longest radio tails: the Frying Pan handle (20 pc), the Mouse (16 pc) and G319.9–0.7 (10 pc), all have very high Mach numbers (200, 60 and 30, respectively; Hales et al. 2009; Kargaltsev et al. 2008) and exhibit smooth morphologies with highly ordered magnetic fields. This indicates a smooth flow structure in these systems, which helps explain the high degree of collimation over long distances.

On the other hand, these three sources show some discrepancies in the detailed morphology and magnetic field structure. The radio emission of the Mouse peaks at the head then gradually fades downstream, and it shows a cone-shaped outer region and a narrow inner region. For the handle of the Frying Pan, the tip is very faint and a two-component structure is not obvious, although the unresolved source at the pulsar position may correspond to the inner region, or the outer region could be too faint to detect. Both the Frying Pan handle and the Mouse have a very similar magnetic field geometry that runs parallel to the tail (Yusef-Zadeh & Gaensler 2005), while G319.9–0.7 shows a B -field perpendicular to the tail (Ng et al. 2010). The origin of this diversity is unclear. It may depend on the pulsar spin orientation relative to its motion or the flow condition of the system. In the regime of high postshock flow speed, the magnetic field may be sheared by the flow so that the field lines are stretched along the tail. More examples are needed to verify this picture. Finally, we note that the polarization vectors in both the Mouse and G319.9–0.7 exhibit abrupt switches at large distances from the pulsar (Yusef-Zadeh & Bally 1987; Ng et al. 2010), which is not observed here. Therefore, we believe that this is not a universal feature among long pulsar tail.

5. CONCLUSIONS

In this paper, we have presented a detailed radio study focusing on the handle of the Frying Pan SNR (G315.9–0.0) using ATCA and MOST observations. Our results confirm the 20 pc-long protrusion as a bow-shock PWN associated with PSR J1437–5959. The detection of both the PWN and the parent SNR makes this system a powerful probe of the pulsar environment. The very small bow-shock stand off distance of 0.002 pc we deduced implies a large pulsar velocity over 1000 km s^{-1} and a high Mach number ~ 200 . The PWN has a highly ordered magnetic field that runs parallel to the tail orientation and has an average strength $\sim 20 \mu\text{G}$. Based on

the pressure estimate and the tail’s opening angle, we found some hints of a small magnetization in the post-shock wind of the order of 0.01–0.1. Also, the ions in the wind could be less energetic than the electrons and positrons. Finally, we suggest that the kink observed in the tail is a result of supersonic ISM turbulence.

As a caveat, the main uncertainties in our derived quantities come from the distance estimate. It is not uncommon for dispersion measure-based distances to be off by 25% or more. While we may have to wait for the Square Kilometer Array for a direct distance measurement with parallax (Smits et al. 2011), multiwavelength studies are essential to further understand the physics of this remarkable system. In particular, X-rays observations can provide a complementary picture of the particle energetics and reveal the flow structure of the highest energy particles. If TeV emission is detected, as in other PWNe, a joint modeling of the synchrotron and inverse Compton scattering emissions can give an accurate measurement of the magnetic field strength. For a pulsar space velocity of 2000 km s^{-1} , a direct proper motion measurement with the ATCA would require a time span over 10 yr. Therefore, other techniques, such as very long baseline interferometry or timing observations, would be more practical. The latter is also essential for a deeper search of γ -ray pulsations in future *Fermi* data.

We thank the referee for careful reading and useful comments. We thank Gemma Anderson to help carry out the 2009 June ATCA observations. The Australia Telescope is funded by the Commonwealth of Australia for operation as a National Facility managed by CSIRO. The MOST is operated by the University of Sydney with support from the Australian Research Council and the Science Foundation for Physics within The University of Sydney.

Facilities: Molonglo Observatory (), ATCA ()

REFERENCES

- Becker, W., et al. 2006, *ApJ*, 645, 1421
 Blondin, J. M., Wright, E. B., Borkowski, K. J., & Reynolds, S. P. 1998, *ApJ*, 500, 342
 Brentjens, M. A., & de Bruyn, A. G. 2005, *A&A*, 441, 1217
 Bucciantini, N., Amato, E., & Del Zanna, L. 2005, *A&A*, 434, 189
 Camilo, F., Ng, C.-Y., Gaensler, B. M., Ransom, S. M., Chatterjee, S., Reynolds, J., & Sarkissian, J. 2009, *ApJ*, 703, L55
 Castelletti, G., Dubner, G., Golap, K., Goss, W. M., Velázquez, P. F., Holdaway, M., & Rao, A. P. 2003, *AJ*, 126, 2114
 Chang, C., Pavlov, G. G., Kargaltsev, O., & Shibanov, Y. A. 2011, *ApJ*, in press, arXiv:1107.1819
 Chatterjee, S., Cordes, J. M., Vlemmings, W. H. T., Arzoumanian, Z., Goss, W. M., & Lazio, T. J. W. 2004, *ApJ*, 604, 339
 Chen, Y., Wang, Q. D., Gotthelf, E. V., Jiang, B., Chu, Y.-H., & Gruendl, R. 2006, *ApJ*, 651, 237
 Cox, D. P. 2005, *ARA&A*, 43, 337
 Dame, T. M., Hartmann, D., & Thaddeus, P. 2001, *ApJ*, 547, 792
 Faucher-Giguère, C.-A., & Kaspi, V. M. 2006, *ApJ*, 643, 332
 Ferrière, K. M. 2001, *Reviews of Modern Physics*, 73, 1031
 Frail, D. A., Giacani, E. B., Goss, W. M., & Dubner, G. 1996, *ApJ*, 464, L165
 Gaensler, B. M., Brazier, K. T. S., Manchester, R. N., Johnston, S., & Green, A. J. 1999, *MNRAS*, 305, 724
 Gaensler, B. M., Chatterjee, S., Slane, P. O., van der Swaluw, E., Camilo, F., & Hughes, J. P. 2006, *ApJ*, 648, 1037
 Gaensler, B. M., & Slane, P. O. 2006, *ARA&A*, 44, 17
 Gaensler, B. M., van der Swaluw, E., Camilo, F., Kaspi, V. M., Baganoff, F. K., Yusef-Zadeh, F., & Manchester, R. N. 2004, *ApJ*, 616, 383
 Gaensler, B. M., & Wallace, B. J. 2003, *ApJ*, 594, 326
 Gvaramadze, V. V. 2006, *A&A*, 454, 239
 Hales, C. A., Gaensler, B. M., Chatterjee, S., van der Swaluw, E., & Camilo, F. 2009, *ApJ*, 706, 1316
 Haverkorn, M., Gaensler, B. M., McClure-Griffiths, N. M., Dickey, J. M., & Green, A. J. 2006, *ApJS*, 167, 230
 Kargaltsev, O., Misanovic, Z., Pavlov, G. G., Wong, J. A., & Garmire, G. P. 2008, *ApJ*, 684, 542
 Lazendic, J. S., Dickel, J. R., Haynes, R. F., Jones, P. A., & White, G. L. 2000, *ApJ*, 540, 808
 Lyutikov, M. 2003, *MNRAS*, 339, 623
 Ng, C.-Y., Gaensler, B. M., Chatterjee, S., & Johnston, S. 2010, *ApJ*, 712, 596
 Ng, C.-Y., Romani, R. W., Brisken, W. F., Chatterjee, S., & Kramer, M. 2007, *ApJ*, 654, 487
 Olbert, C. M., Clearfield, C. R., Williams, N. E., Keohane, J. W., & Frail, D. A. 2001, *ApJ*, 554, L205
 Pacholczyk, A. G. 1970, *Radio Astrophysics. Nonthermal Processes in Galactic and Extragalactic Sources* (San Francisco: Freeman)
 Pavlov, G. G., Teter, M. A., Kargaltsev, O., & Sanwal, D. 2003, *ApJ*, 591, 1157

- Romani, R. W., Shaw, M. S., Camilo, F., Cotter, G., & Sivakoff, G. R. 2010, *ApJ*, 724, 908
- Sault, R. J., Bock, D. C.-J., & Duncan, A. R. 1999, *A&AS*, 139, 387
- Smits, R., Tingay, S. J., Wex, N., Kramer, M., & Stappers, B. 2011, *A&A*, 528, A108
- van der Swaluw, E. 2004, *Advances in Space Research*, 33, 475
- Vigelius, M., Melatos, A., Chatterjee, S., Gaensler, B. M., & Ghavamian, P. 2007, *MNRAS*, 374, 793
- Whiteoak, J. B. Z., & Green, A. J. 1996, *A&AS*, 118, 329
- Wilson, W. E., et al. 2011, *MNRAS*, 416, 832
- Yusef-Zadeh, F., & Bally, J. 1987, *Nature*, 330, 455
- Yusef-Zadeh, F., & Gaensler, B. M. 2005, *Advances in Space Research*, 35, 1129
- Zeiger, B. R., Brisken, W. F., Chatterjee, S., & Goss, W. M. 2008, *ApJ*, 674, 271